J. Fluid Mech. (2000), *vol.* 418, *pp.* 59–76. Printed in the United Kingdom

Turbulent mixing in a sloping benthic boundary layer energized by internal waves

By G. N. IVEY, K. B. WINTERS† AND I. P. D. DE SILVA

Department of Environmental Engineering, Centre for Water Research,
The University of Western Australia, Nedlands, Western Australia 6907

(Received 8 December 1998 and in revised form 2 March 2000)

A laboratory study was carried out to directly measure the turbulence properties in a benthic boundary layer (BBL) above a uniformly sloping bottom where the BBL is energized by internal waves. The ambient fluid was continuously stratified and the steadily forced incoming wave field consisted of a confined beam, restricting the turbulent activity to a finite region along the bottom slope. Measurements of dissipation showed some variation over the wave phase, but cycle-averaged values indicated that the dissipation was nearly constant with height within the BBL. Dissipation levels were up to three orders of magnitude larger than background laminar values and the thickness of the BBL could be defined in terms of the observed dissipation variation with height. Assuming that most of the incoming wave energy was dissipated within the BBL, predicted levels of dissipation were in good agreement with the observations.

Measurements were also made of density and two orthogonal components of the velocity fluctuations at discrete heights above the bottom. Cospectral estimates of density and velocity fluctuations showed that the major contributions to both the vertical density flux and the momentum flux resulted from frequencies near the wave forcing frequency, rather than super-buoyancy frequencies, suggesting a strong nonlinear interaction between the incident and reflected waves close to the bottom. Within the turbulent BBL, time-averaged density fluxes were significant and negative near the wave frequencies but negligible at frequencies greater than the buoyancy frequency N. While dissipation rates were high compared to background laminar values, they were low compared to the value of $\varepsilon_{tr} \approx 15\,\nu N^2$, the transition value often used to assess the capacity of a stratified flow to produce mixing. Existing models relating mixing to dissipation rate rely on the existence of a positive-definite density flux at frequencies greater than N as a signature of fluid mixing and therefore cannot apply to these experiments. We therefore introduce a simple model, based on the concept of diascalar fluxes, to interpret the mixing in the stratified fluid in the BBL and suggest that this may have wider application than to the particular configuration studied here.

1. Introduction

Quantifying the dynamical processes in the benthic boundary is of fundamental interest both in oceanography and limnology. It is believed, for example, that the vertical transport of mass in the benthic layer may account for the discrepancy between vertical exchange rates determined from large-scale budget calculations and

† Also at Applied Physics Laboratory, University of Washington, Seattle, WA 98105-6698, USA.

the lower estimates inferred from direct turbulent microstructure measurements in the interior of lake and ocean basins (e.g. Munk & Wunsch 1998). Turbulence in the benthic boundary layer can also play a central role in the transport of nutrients, sediment and biological material into the interior fluid via the formation of baroclinic horizontal intrusions (e.g. De Silva, Imberger & Ivey 1997, hereafter referred to as DII). Field experiments in both the ocean (e.g. Eriksen 1982, 1985; Wolanski 1987; Thorpe, Hall & White 1990; Toole, Polzin & Schmitt 1994; White 1994; Van Haren, Oakey & Garrett 1994; Ledwell & Hickey 1995) and in lakes (Imberger & Hamblin 1982; Wuest *et al.* 1994; Lemckert & Imberger 1995) have been designed to investigate these processes. Benthic turbulence is known to result from a variety of mechanisms, including flow over topographically rough terrains, river inflows, basin-scale seiches, and the breaking of internal gravity waves. In this work, we consider turbulence generated by the breaking of internal gravity waves impinging on a sloping bottom.

In the linear limit, an internal gravity wave of frequency ω propagates through a stratified fluid of buoyancy frequency N at an angle $\alpha = \sin^{-1}(\omega/N)$ to the horizontal. Here $N^2 = -(g/\rho_0)\partial\rho/\partial z$ where $\rho(z)$ is the ambient density profile after complete relaxation and ρ_0 is a reference density. The presence of the solid bottom results in a reflected wave with the same intrinsic wave frequency as the incident wave. Linear internal wave reflection off a sloping bottom in the two-dimensional case has been treated analytically by Phillips (1977). Eriksen (1985) extended the analysis to obliquely incident waves while Thorpe (1987) considered finite-amplitude internal waves. DII introduced a geometric parameter $\gamma = \sin\alpha/\sin\beta$ where α is the angle of the wave vector and β is the angle the sloping bed makes with the horizontal, both relative to the horizontal. For critically incident waves when $\gamma = 1(\omega = N\sin\beta)$, the linear, inviscid analysis becomes singular and large amplitudes of the reflected wave are predicted. The critical case has thus received most attention. However, Ivey, De Silva & Imberger (1995) and DII found that when $\gamma > 1$, turbulent mixing can be expected for a wide parameter range and can be more intense in this range than for the critical case when $\gamma = 1$.

Despite the importance of the process, only a handful of laboratory experiments have examined the process of internal wave reflection at sloping beds (Cacchione & Wunsch 1974; Ivey & Nokes 1989, 1990; Taylor 1993; DII; Michallet & Ivey 1999). DII showed that boundary mixing driven by internal wave reflection could be viewed as an interaction between the incident and reflected wave fields. For an incident wave beam of finite width, this interaction occurs primarily in the triangular region defined by the superposition of incident and reflected wave beams. Flow visualization and particle velocimetry by DII showed that, near critical conditions, the turbulence was confined to a thin narrow region just above the bottom where most of the incident wave energy was dissipated with relatively small overturning lengthscales. More vigorous mixing, and larger overturning lengthscales, were observed in the range $1.5 < \gamma < 2$, consistent with previous laboratory experiments reported by Ivey & Nokes (1990) and Ivey *et al.* (1995). In the present laboratory study, we extend these earlier studies by directly measuring turbulence properties, in particular the turbulent fluxes of mass and momentum, in the benthic boundary layer energized by internal waves.

We describe the laboratory experiments in § 2, followed by the presentation of the dissipation and flux measurements in § 3. In § 4, we interpret these measurements in the light of existing models which relate mixing to dissipation rates. As we show, it is difficult to reconcile our observations with existing models, and we therefore present in § 4.2 an alternative model of mixing, based on the concept of diascalar fluxes, which

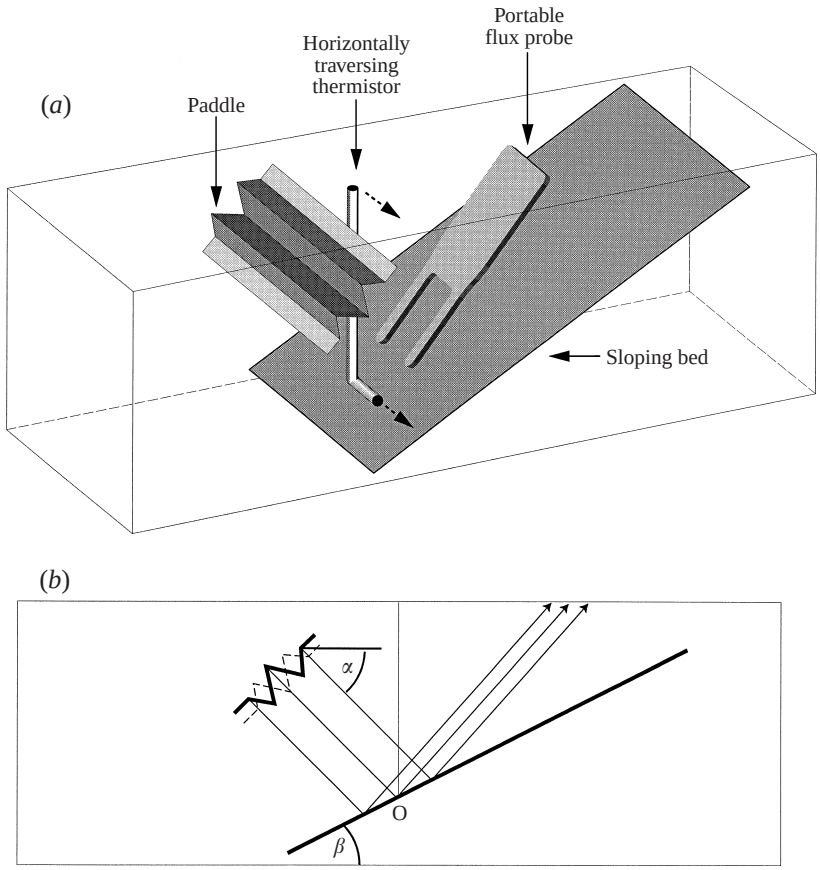

FIGURE 1. (*a*) Schematic of the laboratory set-up showing the configuration of the paddle, horizontally traversing thermistor probe and location of flux probe to measure *in situ* turbulent fluxes. (*b*) Definition of bottom slope and wave ray slope.

is consistent with the present observations. This model cannot be comprehensively tested in the present experiments, but as outlined in § 4.2 and in the conclusions in § 5, it is offered both as a testable hypothesis for future work and to stimulate discussion on the principles underlying mixing rates in stratified fluids.

2. Experiments

2.1. *Experimental facility and the instrumentation*

The experimental facility consisted of a glass-walled tank 590 cm long, 54 cm wide and 60 cm deep (DII). The experiments were done in a 3 m long partitioned portion of this tank to reduce the total volume of the fluid. A 12 mm thick Plexiglas sheet, pivoted as its centre point and with the pivot point mounted 12 cm above the tank bottom formed a uniform sloping bed. The internal wave rays were generated using a multi-bladed folding paddle, made up of eight separate hinged blades free to pivot independently about their long central axis. Each blade was 5 cm wide by 53.5 cm long, extending over the entire width of the tank. The blades could be moved by a series of rods connected to an eccentric wheel driven by a precision DC motor. When oscillated the system formed an oscillating M or W shape (for details see DII; Teoh,

Ivey & Imberger 1997 and figure 1). The wavelength in the plane of the paddle was thus 20 cm and the amplitude of the blade oscillation was kept constant at 3.1 cm.

For the experiments described in this paper, the paddle assembly used by DII was re-designed so that the entire structure could be pivoted to a required angle α. This arrangement was chosen for two reasons: first, with the new arrangement, the paddle blades force the fluid particles to travel in the preferred direction of the wave ray which reduces mixing due to paddle forcing and, secondly, only one ray tube is produced so that most of the paddle energy is imparted to the intended beam. In this way, when the paddle was oscillated only a single beam of internal waves could be generated – a beam which propagated away from the paddle perpendicular to the plane of the paddle. With this configuration, a single beam of internal waves oriented at predetermined angles with respect to the bed could be readily excited (see figure 1).

2.2. *Experimental procedure*

The tank was filled with a linearly stratified salt solution to a depth of 50 cm and while there were inevitably small temperature variations in the vertical associated with the filling, temperature is effectively a passive tracer. The wave paddle assembly was then fixed in position, adjusted to the desired orientation, and the wave motion initiated by oscillating the blades forming the wave paddle. Typical experimental runs lasted about 5 minutes. While data were recorded throughout a run, our analyses are confined to the steady regimes well after the initial transients. Depending on the experiment, measurements were made in one of two different modes: either a profiling mode in which the sensors were traversed through the fluid or a time series mode in which the sensors were held at a fixed location.

Profiling was carried out using both vertical and horizontal traverses. Vertical measurements of the temperature and conductivity were recorded to obtain the vertical density profile. This was accomplished using three probes: a fast-response Precision Measurement Equipment four-electrode microscale conductivity probe, a siphoning conductivity probe, and an FP07 thermistor for temperature. The siphoning probe was used to provide dynamic calibration for the fast-response conductivity probe. The spacing between the tips of the three sensors was less than 4 mm. The probe assembly was mounted on a computer-driven platform with a traversing speed of $10\,\mathrm{cm\,s^{-1}}$. Direct and differentiated output from each sensor was recorded at 100 Hz via a 16-bit A/D converter.

Estimates of the rate of dissipation of turbulent kinetic energy ε were made by measuring the gradient of the temperature signal along horizontal traverses and fitting the theoretical Batchelor spectrum (see § 3.1). While the density variation was due to the salinity variation, there were always small variations in the temperature resulting from the filling process and slight fluctuations in the laboratory air temperature over time. Current sensor technology does not allow measurements out to the dissipation range in the salinity field, but it is possible in the temperature field. Previous work in similar configurations (Teoh *et al.* 1997; DII) indicated that with a spatial resolution of about 1 mm such measurements obtained from vertical profiling yield relatively small record lengths for typical laboratory-scale turbulent events. In the present experiments, the thermistor sensor was traversed horizontally at a constant height laterally across the width of the tank – thereby taking advantage of the two-dimensional nature of the wave created by the uniform paddle forcing across the tank width. The traversing speed was set at $10\,\mathrm{cm\,s^{-1}}$ and the technique yielded record lengths of 256 mm, or 256 points, for the spectral analysis. The time taken to obtain a complete record was short compared to typical wave periods. The method had the dual advantages

Run	α (deg.)	β (deg.)	N (rad^{-1}s)	γ
1	47	20	0.68	2.15
2	48	36	0.73	1.26
3	41	10	0.74	3.76
4	44	25	0.70	1.67
5	50	22	0.74	1.91
6	37	22	0.74	1.52
7	37	10	0.74	3.46
8	37	10	0.74	3.28
9	37	15	0.74	2.19
10	37	25	0.74	1.35
11	37	25	0.74	1.34

TABLE 1. Summary of experimental runs. Angles are defined in figure 1(*b*).

of not only yielding longer record lengths, and hence better fits with the theoretical spectrum, but also permitted investigation of the spatial variation of dissipation ε with distance above the bottom at very fine resolution – starting as little as a few mm off the bottom.

The time series measurements were made from the commencement of paddle motion with the Portable Flux Profiler (PFP) (described by Imberger & Head 1994 and originally designed for use in the field). The instrument is equipped with duplicate pairs of FP07 thermistors and fast-response conductivity sensors, and a laser Doppler anemometer measuring two orthogonal components of velocity with a resolution of 0.001 m s^{-1} on each channel. The temperature and conductivity sensors were separated by 2.5 mm in the horizontal, the time response and resolution of the temperature sensor were 12 ms and 0.001°C, while those of the conductivity probe was 4 ms and 0.0004 S m^{-1}, respectively. While the density variation in the vertical was dominated by the salinity variation, with this accuracy of temperature resolution we were easily able to resolve the gradient temperature signals due to the small background or mean temperature variations inevitably resulting from the filling process. The temperature and conductivity signals from the PFP were filtered using a recursive filter (sharpened and smoothed) to match the differences in time responses. Further details regarding the instrument can be found in Imberger & Head (1994), Saggio & Imberger (2000) and Etemad-Shahidi & Imberger (1998).

The PFP was mounted on an assembly attached to two rails running along each side of the tank. The assembly allowed for vertical adjustments so that the measurement volume of the probe could be positioned at a prescribed height above the sloping bottom. With the wave paddle placed at an angle α to the horizontal, the centre of the emanating wave ray was directed at the hinge point O (see figure 1). The measurements were taken along the vertical centreline through the hinge point. To achieve measurements close to the bed, the PFP had to be inclined to the vertical at an angle of 37°. The probe itself was placed upslope of the hinge point and all runs were confined to the supercritical case to minimize the unwanted effects associated with flow passing around the probe. Turbulent fluxes of both mass and momentum were obtained via time series records of two orthogonal velocity components, temperature and conductivity, typically recorded for a period of about 5 minutes after the initiation of wave forcing.

A summary of the runs conducted listing the experimental parameters is shown in table 1.

3. Results

3.1. *Dissipation measurements*

The dissipation of turbulent kinetic energy ε was obtained by fitting a theoretical Batchelor spectrum (Batchelor 1959) for the temperature gradient to the measured temperature gradient spectra, taking ε as a free parameter. While conductivity measurements were also made, the conductivity sensor is unable to resolve down to the salinity dissipation scales, so we only use the temperature gradient signal in subsequent processing. This technique has been successfully used both in the field (e.g. Imberger & Ivey 1991) and in laboratory studies (e.g. DII; Teoh *et al.* 1997; Grigg & Ivey 1997). Temperature sensor resolution limits measurement of dissipation values to a low value of around $10^{-10}\,\mathrm{m^2\,s^{-3}}$ (e.g. Etemad-Shahidi & Imberger 1998; Luketina & Imberger 1999), much less than the observed dissipation levels in the BBL. Using typical experimental parameters, a wave amplitude $a = 0.01\,\mathrm{m}$, a wavenumber $k = 5\ \mathrm{rad\,m^{-1}}$ and a forcing frequency $\omega = 0.5\ \mathrm{rad\,s^{-1}}$, yields an estimate of the dissipation rate induced by the laminar wave as $\varepsilon_{wave} - \nu(ak\omega)^2 - 10^{-9}\,\mathrm{m^2\,s^{-3}}$; just above the instrument noise level. Calibration testing (M. Barry, personal communication) has shown that at probe traversing speeds of $10\,\mathrm{cm\,s^{-1}}$, the upper limit of the dissipation estimates is around $6\times10^{-6}\,\mathrm{m^2\,s^{-3}}$, while repeated sampling of the same flow indicates that the accuracy of dissipation estimates is $\pm30\%$ (where the error bound represents ±1 standard deviation) throughout the range from this high end value down to the low end at $10^{-10}\,\mathrm{m^2\,s^{-3}}$.

Flow visualization by DII showed that, owing to the nature of the paddle design and the experimental geometry, the flow field is nearly two-dimensional outside the BBL. Within the BBL, the signatures of small-scale turbulence are superimposed on the nearly two-dimensional background wave field. One thus expects a variation in the dissipation rate with height from the bottom. Ivey *et al.* (1995) considered a simple energy balance in the wave interaction region for critical waves ($\gamma = 1$) and this can be readily extended for the present case with $\gamma \neq 1$.

For an internal wave train in two dimensions, linear theory (e.g. Phillips 1977) indicates that the velocity and density perturbations are described by

$$u = -w_0 \sin\alpha \cos(kx + mz - \omega t), \tag{1a}$$

$$w = w_0 \cos\alpha \cos(kx + mz - \omega t), \tag{1b}$$

$$\rho = -\frac{w_0}{g\omega}\rho_0 N^2 \cos\alpha \sin(kx + mz - \omega t), \tag{1c}$$

where u and w are the horizontal and vertical (positive upward) velocities, k and m are the horizontal and vertical wavenumbers, w_0 is the maximum particle speed and α the angle of the group velocity vector to the horizontal. The average over one wave period of the incident vertical energy flux passing through a horizontal surface with dimensions of one wavelength in the x-direction (and per unit width in y) is then

$$E_i = \frac{\pi}{k}\rho_0 w_0^2 C \sin\alpha, \tag{2}$$

where the phase speed $C = \omega/(k^2 + m^2)^{1/2}$.

The reflected energy is given by $E_r = rE_i$ where r is the reflection coefficient. The average dissipation rate over a wave cycle in a turbulent mixing layer of thickness h adjacent to the bottom is then given by

$$\bar{\varepsilon} = \frac{E_i - E_r}{\rho_0 hl} = \frac{(1-r)E_l}{\rho_0 hl}. \tag{3}$$

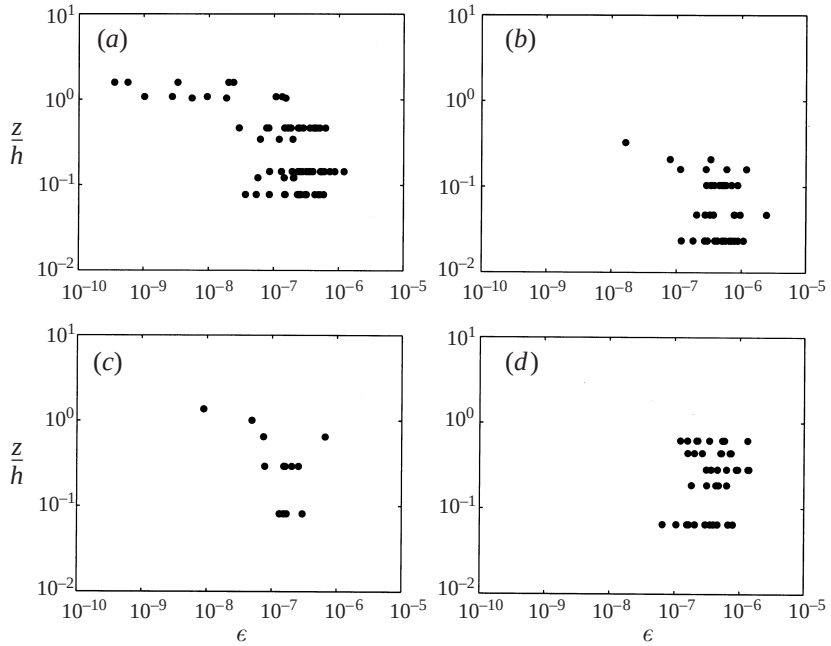

FIGURE 2. Measured dissipation $\varepsilon\,(\mathrm{m^2\,s^{-3}})$ as a function of height for runs 1–4 (*a–d*). The perpendicular distance from the slope is non-dimensionalized by the estimate of benthic boundary layer thickness in equation (4). Dissipation estimates are $\pm 30\%$.

In equation (3), l is the maximum length along the slope over which any energy dissipation could occur, and this is determined by the width of the incident and reflected wave beams and the geometry, implying that the length $l = (2\pi \sin\alpha)/k \sin(\alpha + \beta)$ (see figure 1). From published laboratory data for the critical case, Ivey *et al.* (1995) showed that the thickness $h = (0.10 - 0.15)\lambda_p$, where λ_p is the wavelength of the incident wave measured in the direction perpendicular to the bottom slope, and h was estimated from either visual observation or microstructure profiles in the vertical which recorded vertical overturn scales. Assuming for the moment that the same condition applies for all waves with $\gamma > 1$, then we may write

$$h = 0.1 \frac{2\pi}{\sqrt{k^2 + m^2}\cos(\alpha + \beta)}, \tag{4}$$

where we have chosen the lower bound for the coefficient. Substituting (4) into (3) and using $l = (2\pi \sin\alpha)/k \sin(\alpha + \beta)$, we obtain an expression for the cycle-average dissipation $\bar{\varepsilon}$ in the benthic layer in terms of external wave parameters as

$$\bar{\varepsilon} = 0.4(1 - r)w_0^2 N \cos\alpha \sin 2(\alpha + \beta), \tag{5}$$

The measured dissipation rates are shown as a function of height from the bottom in figure 2 for four runs with γ ranging from 1.4 to 2.2. Distance from the bottom is non-dimensionalized by the estimate of benthic layer height in equation (4). Close to the bottom, dissipation estimates are as high as $10^{-6}\,\mathrm{m^2\,s^{-3}}$ and decrease to levels as low as $10^{-9}\,\mathrm{m^2\,s^{-3}}$ far from the bottom. Despite numerous attempts, it was difficult to obtain dissipation estimates from Batchelor fitting techniques far from the bottom because the background flow was non-turbulent laminar internal wave motion. At any particular elevation above the slope, dissipation varies in successive estimates due

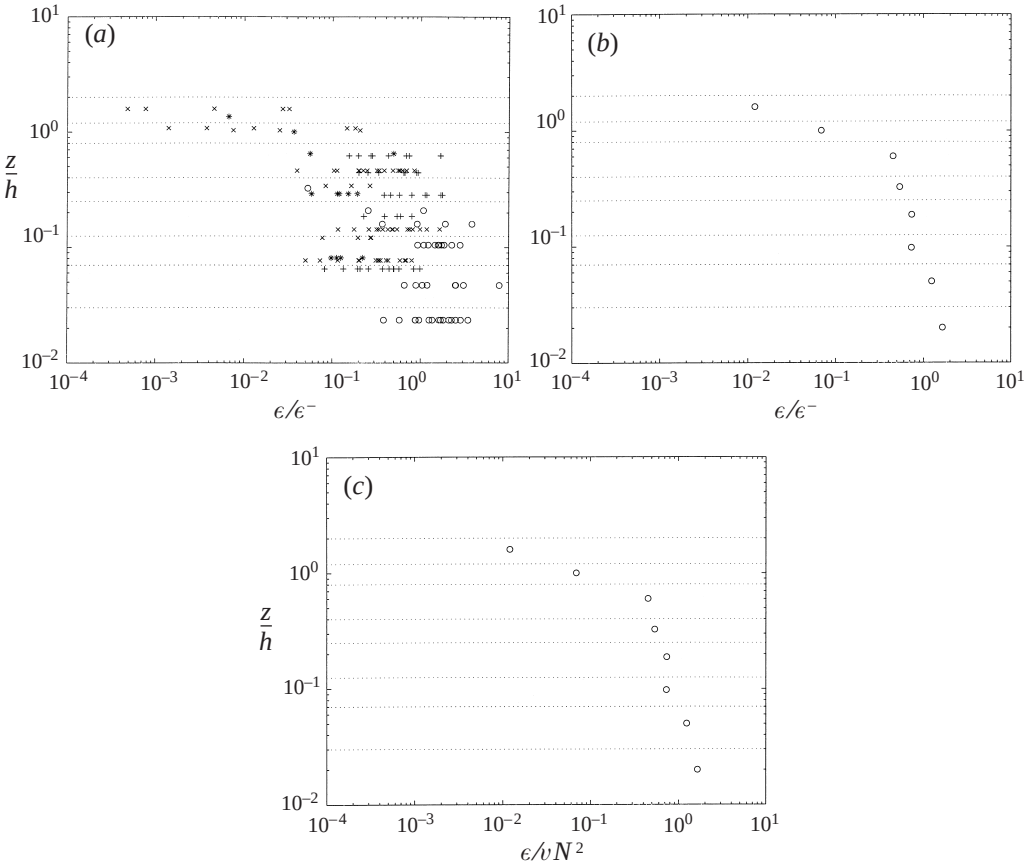

FIGURE 3. (*a*) Dissipation data from all the runs in figure 2 with vertical bins as shown. (*b*) Bin-averaged data. Height is non-dimensionalized by the estimate of benthic boundary layer height in equation (4) and all dissipation estimates are non-dimensionalized by the estimate of dissipation in equation (5). (*c*) Bin-averaged dissipation non-dimensionalized by νN^2 for all data shown in figure 2.

to wave phase – a feature noted in earlier experiments by Ivey & Nokes (1989), for example.

In figure 3(*a*), the data from the various runs are combined by non-dimensionalizing the measured dissipations by the cycle-averaged values in equation (5), where we assume for the moment that the reflection coefficient $r = 0$ (see below). Data were binned according to the bin sizes shown in figure 3(*a*) and the phase- and bin-averaged values are shown as a function of height in figure 3(*b*). As can be seen from figure 3(*b*), the dissipation is nearly constant over the benthic layer height h, and beyond that it decreases rapidly with increasing height, approaching the background levels typical of the incident linear wave field. The thickness of the boundary layer, determined here in terms of the spatial variation of dissipation ε, is well described by (4) despite the fact that the BBL thickness estimated by Ivey *et al.* (1995) was based on very different measures of the turbulence field. The best-fit coefficient in equation (4) was 0.08; it was rounded to 0.1 in accord with the previous results from the critical case. The most notable feature from figure 3(*b*) is that the measured values of dissipation are in close agreement with the cycle-average predicted dissipation in equation (5).

The close accord between model predictions and observations suggests that the underlying assumptions made in deriving the model are reasonable. As can be seen from figure 3(*b*), the observed dissipations are slightly less than the predicted dissipations obtained by assuming $r = 0$. Measured values of dissipation averaged over the BBL are approximately 70% smaller, implying that the best estimate of the reflection coefficient in (5) is $r = 0.3$. Much of the incident wave energy was clearly lost in a single reflection from the bottom and little energy escapes the BBL, even when the incident waves are slightly supercritical as in the present case.

Finally, in figure 3(*c*), we plot the quantity $(\varepsilon/\nu N^2)$ as a function of height. When the dissipation rate is small enough that $(\varepsilon/\nu N^2) = (L_0/L_K)^{4/3} \leqslant 15$, results from laboratory experiments (e.g. Itsweire, Helland & Van Atta 1986) and field experiments (e.g. Saggio & Imberger 2000) indicate that an irreversible downgradient turbulent density flux is no longer sustained. In this limit, the Ozmidov scale $L_O = (\varepsilon/N_*^3)^{1/2}$ and the Kolmogorov scale $L_K = (\nu^3/\varepsilon)^{1/4}$ are comparable, hence there is no bandwidth of turbulent overturning scales able to support a density flux. In the present experiments $(\varepsilon/\nu N^2) = 1$ within the boundary layer, a value typical of measurements made in earlier wave–bottom interaction experiments by DII, and wave–wave interaction experiments by Teoh *et al.* (1997). In the present case, with wave-forced turbulence, there is an input into the velocity and density fields at the internal wave scale a and it is thus of interest to examine the measured density flux in the light of the results in figure 3(*c*).

3.2. *Density flux measurements*

Variance-preserving cospecta (e.g. Bendat & Piersol 1966) of density and vertical (positive upwards) velocity $Co_{\rho w}$ are shown in figure 4 at four different heights for some typical runs. For each run, the measurement height is non-dimensionalized by the benthic boundary layer thickness in equation (4). In all cases, the records were close to the bottom and individual signals consist of a superposition of incoming and reflected wave rays. A negative value of the cospectrum indicates transport leading to re-stratification, whereas a positive value indicates downgradient transport. The clearest feature for all heights shown in figure 4 is that the density flux is centred on the forcing frequency ω_f, indicating the nonlinear nature of the wave field. The magnitude of this re-stratifying buoyancy flux is comparable inside and outside the boundary layer, although there is some weakening of this flux for $z < 0.2\,h$. The sign of the density flux is always negative, however, indicating re-stratification. This re-stratifying density flux associated with wave–wave interactions is evidently part of a secondary flow on a scale larger than that defined by the turbulent BBL. Such a flow is illustrated in DII's figure 15, for example, with slow flow out from the boundary region and a compensating return flow above and below the outflow.

It is tempting to assume that the contribution to the density flux from frequencies above the frequency N is due to turbulence, while that between the paddle frequency and N is due to the wave motions. In this case, however, care is required due to the possibility of Doppler shifting. With some caution therefore in regard to the exact limits of integration, the contribution to the buoyancy flux $b = -(g/\rho_0)\overline{\rho' w'}$ due to turbulent motions alone can be defined as (e.g. Sun, Kunze & Williams 1996)

$$b = -\frac{g}{\rho_0}\int_N^\infty Co_{\rho w}\,\mathrm{d}\omega. \tag{6}$$

As can be seen from figure 4, irrespective of either the position in the BBL or the

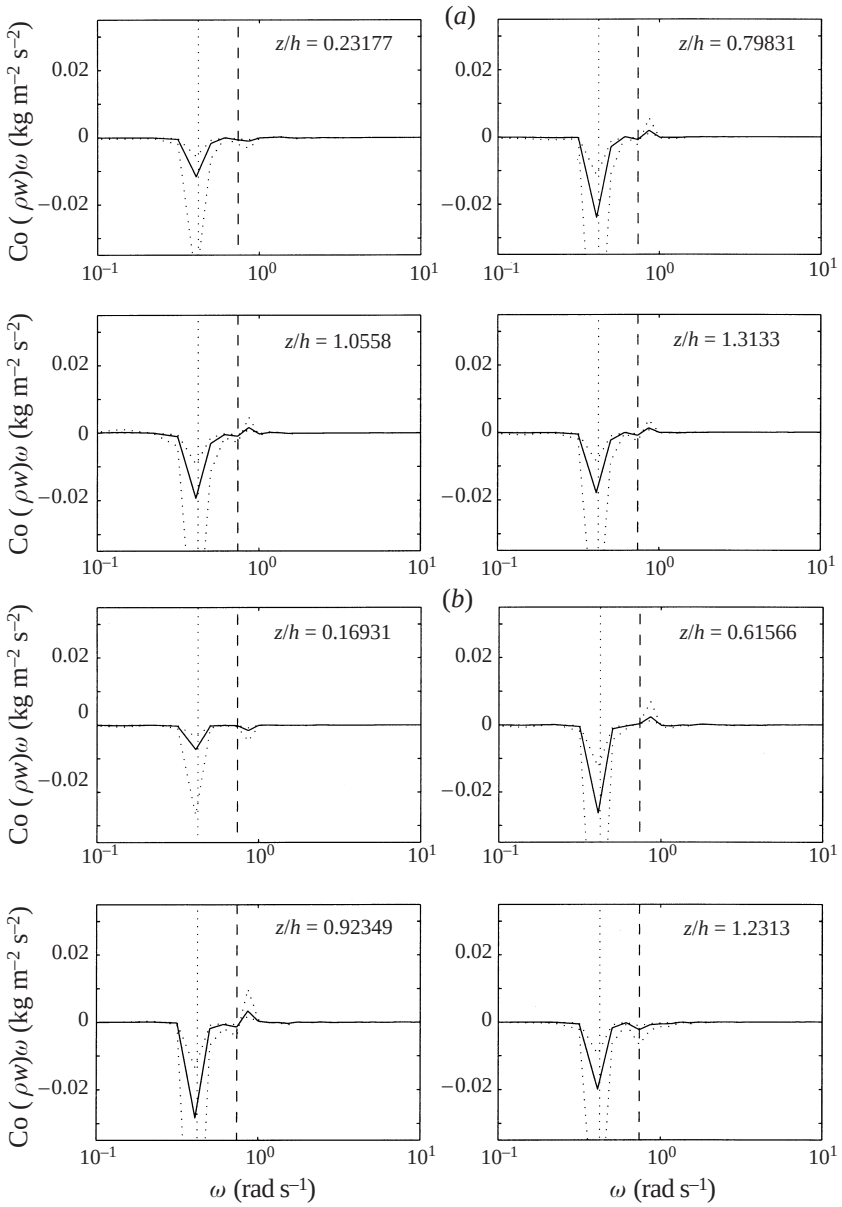

FIGURE 4. Cospectra of density and vertical velocity, in variance-preserving form, obtained from four different heights from the bottom for two typical runs: (*a*) run 6 and (*b*) run 9. The dashed vertical line corresponds to the buoyancy frequency, and the dotted vertical line to the wave forcing frequency ω_f. Confidence limits are shown as dotted lines. The height h refers to the prediction for the benthic boundary layer height in equation (4). The accuracy of buoyancy flux measurements is $\pm 15\%$.

value of the criticality parameter γ, the density or buoyancy flux is small, certainly negligibly small compared to the flux values near the forcing frequency.

The density flux is thus dominated by the wave contribution. From figures 3 and 4, inside the BBL we have a region of both enhanced turbulent dissipation and enhanced departure from linear wave behaviour compared to background levels. The

dissipation is dominated by contributions from high wavenumbers and frequencies, and uncorrelated with the observed density flux which is predominantly at the frequency ω_f. The internal wave contribution to dissipation is always negligibly small (even in a nonlinear wave field) compared to the measured values $\varepsilon_{max} \approx 10^{-6}\,\mathrm{m^2\,s^{-3}}$. This implies that frequencies with $\omega \geqslant N$ dominate the observed dissipation rates. The lack of a significant positive or downgradient density flux at frequencies $\omega > N$ in figures 3 and 4 is consistent with the observation that $(\varepsilon/\nu N^2) \approx 1$, but leads to a rather fundamental question. Given that the dissipation ε is so high (nearly 10^3 times the background laminar internal wave levels in figure 3*b*), does the lack of local positive density flux really imply that there is no local irreversible mixing? We suggest not, and explore this issue in more detail in § 4.

3.3. *Reynolds stress*

For completeness, in figure 5 we show the corresponding variance-preserving cospectra of horizontal and vertical velocity Co_{uw} for the runs in figure 4. The dominant contribution to the Reynolds stress occurs at ω_f where $\overline{uw} < 0$ both inside and outside the BBL. As with the density flux, there is little contribution to the Reynolds stress for frequencies greater than the buoyancy frequency N.

4. Discussion of results

The results above suggest that density fluxes at high frequencies (i.e. $\omega > N$) are not a good indicator of irreversible mixing. For example, Itsweire *et al.* (1986) argued that only if $\varepsilon > 15\nu N^2$ could one observe a positive downgradient density flux. In our case with $(\bar{\varepsilon}/\nu N^2) \approx 1$ we observe significant non-zero fluxes within the BBL near ω_f. In wave-forced turbulence, energy is supplied to the flow at the scale $L = a$ (wave amplitude) in both the density and velocity fields. In our case with $a > L_K$ (the Kolmogorov scale), density fluxes are dominated by scale a. Depending on the degree of nonlinearity of the waves, there is always the potential for density flux contributions near the largest scales of the forced motion.

4.1. *Eddy diffusivity from buoyancy flux*

Osborn (1980) showed if one defined an eddy diffusivity K_ρ in terms of buoyancy flux b as

$$K_\rho = \frac{(g/\rho_0)\overline{\rho' w'}}{N^2} = -\frac{b}{N^2}, \tag{7}$$

then, from a simplified form of the turbulent kinetic energy equation, the diffusivity is

$$K_\rho = \left(\frac{R_f}{1 - R_f}\right)\frac{\varepsilon}{N^2}, \tag{8}$$

where the flux Richardson number R_f is a measure of the mixing efficiency.

This model has some limitations, however, as can be seen by considering an example of mixing in a salt-stratified system. Ivey, Imberger & Koseff (1998) showed that the maximum value of $R_f \approx 0.25$, implying from (8) that the maximum value of $K_\rho \approx 0.33(\varepsilon/N^2)$. For dissipation levels just above the transition value of $\varepsilon = 15\nu N^2$, this implies that the effective diffusivity is $K_\rho \approx 5\nu = 5 \times 10^{-6}\,\mathrm{m^2\,s^{-1}}$. Conversely, when the dissipation is slightly below the transition value of $\varepsilon = 15\nu N^2$, the buoyancy flux b is zero (e.g. Itsweire *et al.* 1986). This implies that K_ρ must also be zero according to the definition in (7), and the effective diffusivity must therefore revert

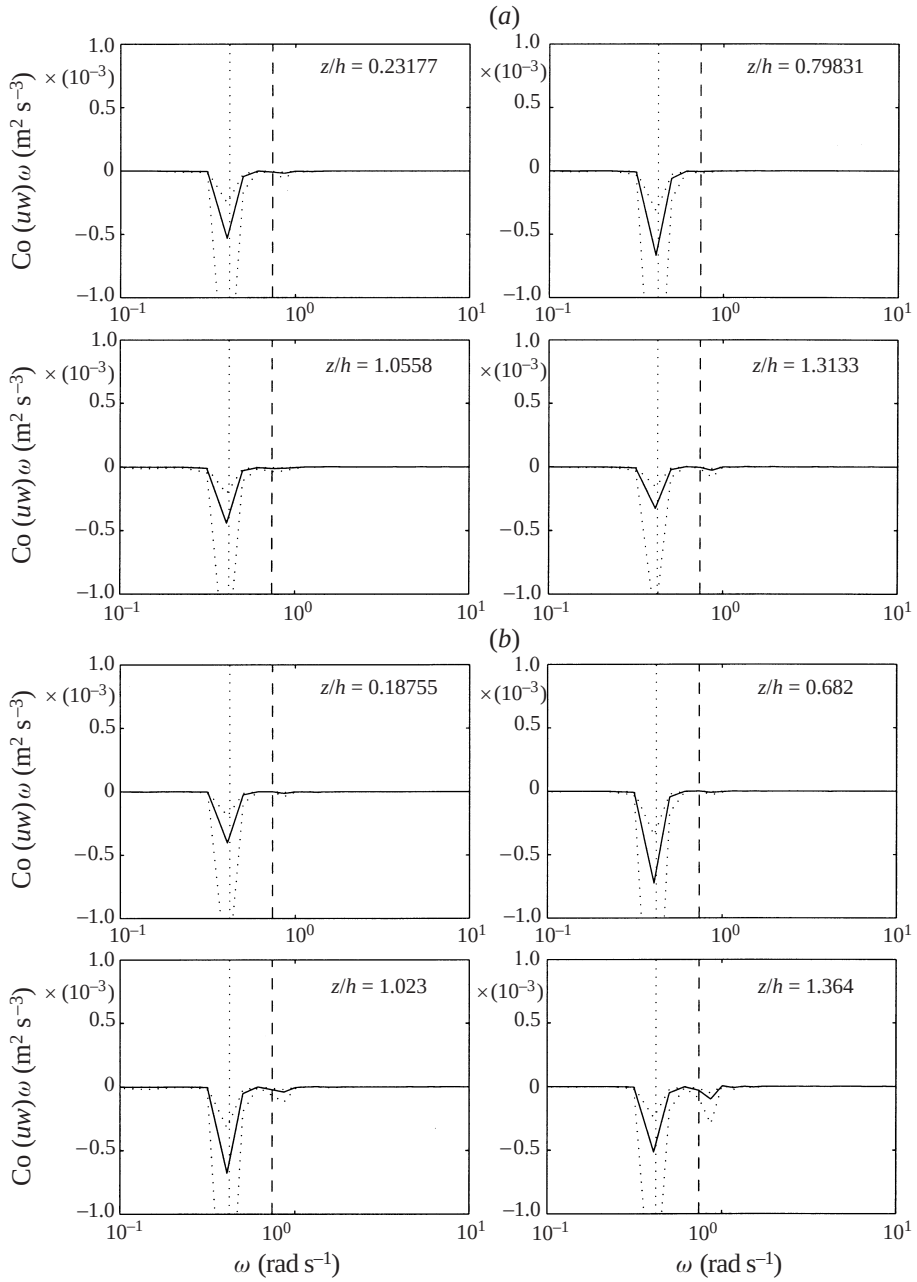

FIGURE 5. As figure 4 but for cospectra of horizontal and vertical velocity. The accuracy of the Reynolds stress is $\pm 30\%$.

to the molecular value of $10^{-9}\,\mathrm{m^2\,s^{-1}}$. It seems implausible that, when there are no other transitions in the flow, a small change in the dissipation rate ε could result in the effective diffusivity changing by three orders of magnitude.

This example suggests that the model in (7) and (8) is unable to describe all the features we expect to see in turbulence in a stratified fluid. In particular, we suggest that the buoyancy flux b may not always be a robust signature of mixing, hence

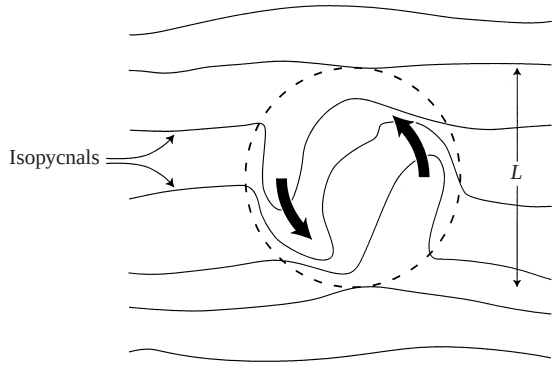

FIGURE 6. Schematic of the wrapping of isopycnal surfaces in a density-stratified fluid due to the action of an eddy of scale L. Density difference between isopycnals across the eddy is $|\mathrm{d}\rho/\mathrm{d}z|L$.

defining the eddy diffusivity K_ρ in terms of buoyancy flux b can be misleading. Rather, the eddy diffusivity should be defined in an alternative way, and we propose such a model in the section below.

4.2. *Eddy diffusivity from diascalar flux*

The average diffusive or diascalar flux F passing across an isopycnal surface S is given by (Winters & D'Asaro 1996)

$$F = \frac{1}{A}\int_S \kappa \nabla\rho \cdot \hat{\boldsymbol{n}}\mathrm{d}S = \frac{1}{A}\int_S \kappa|\nabla\rho|\mathrm{d}S = \frac{\langle|\nabla\rho|\rangle^2}{|\mathrm{d}\rho/\mathrm{d}z_*|}\kappa, \tag{9}$$

where z_* is an isoscalar coordinate with dimensions of length, the angled brackets indicate the spatial average over the surface S, κ is the molecular diffusivity of the stratifying species and A is the geometrical projection of S onto a horizontal plane. The corresponding value of the eddy diffusivity K_ρ is

$$K_\rho = \frac{F}{|\mathrm{d}\rho/\mathrm{d}z_*|} = \frac{\langle|\nabla\rho|\rangle^2}{|\mathrm{d}\rho/\mathrm{d}z_*|^2}\kappa. \tag{10}$$

Consider a density-stratified fluid with Prandtl number $Pr > 1$ and an ambient (i.e. adiabatically re-sorted) density gradient $\mathrm{d}\rho/\mathrm{d}z_*$, with turbulent motions characterized by fluctuations in the density field with a displacement scale L. The density difference between fluid parcels within such structures is thus of order $|\mathrm{d}\rho/\mathrm{d}z_*|L$ (see figure 6). As shown schematically in figure 6, the straining or 'wrapping' motion at scale L will result in a convergence of isopycnal surfaces. The separation distance $\Delta x_l (i = 1, 2, 3)$ between two such isopycnal surfaces thus decreases until it becomes comparable to the Batchelor scale $L_B = L_K/Pr^{1/2}$, and at this scale molecular diffusion smooths the locally enhanced gradients. Since the scalar gradient spectra is blue, that is the variance is concentrated at the smallest allowable scales or highest wavenumbers (i.e. the Batchelor scale), this simple model implies that the characteristic magnitude of the density gradient in (10) will be given by

$$\langle|\nabla\rho|\rangle \sim \frac{\Delta\rho}{\Delta x_i} \sim \frac{|\mathrm{d}\rho/\mathrm{d}z_*|L}{L_B}. \tag{11}$$

Substituting (11) into (10) yields a scaling estimate of the diascalar diffusivity

$$K_\rho \sim \left(\frac{L}{L_B}\right)^2 \kappa. \tag{12}$$

In general, the characteristic displacement scale L will depend on both fluid and flow properties. We outline below a number of distinct regimes, ranging from laminar flow to energetic density–stratified turbulence, and in each regime we make estimates of L and hence of the expected value of K_ρ.

4.2.1. *Laminar flow*

By definition, there is no turbulent motion in this regime. There are nevertheless perturbations to the background density field with a characteristic displacement scale L. The magnitude of the density gradients associated with these perturbations is not appreciably greater than the background gradient, that is $\langle|\nabla\rho|\rangle \sim |\mathrm{d}\rho/\mathrm{d}z_*|$ or equally $L \sim L_B$ and hence (12) reduces to $K_\rho \sim \kappa$, as required.

4.2.2. *Density-stratified turbulence*

As shown by Batchelor (1959), in the absence of buoyancy effects (as would be the case for a passive tracer, for example) scales smaller than the Kolmogorov lengthscale L_K are affected only by a uniform straining motion with strain rate $(\varepsilon/\nu)^{1/2}$, or equivalently the straining motion has a characteristic timescale $T_S \sim (\nu/\varepsilon)^{1/2}$ In a density-stratified turbulent flow, however, buoyancy should be important at these scales if the buoyancy timescale $T_b \sim N_*^{-1}$ is small compared to T_S, where N_* refers to the buoyancy frequency based on the re-sorted density gradient $\mathrm{d}\rho/\mathrm{d}z_*$. The requirement that $T_b < T_S$ is equivalent to the requirement $\varepsilon < \nu N_*^2$. This implies that the displacement scale L, characterizing the largest overturning scales in the density field, must therefore be a function of ε, ν and N_*. If we assume that L increases with an increase in the dissipation ε and decreases with an increase in N, then dimensional reasoning implies that

$$L \sim (\nu\varepsilon)^{1/4}/N_*. \tag{13}$$

One interpretation of (13) is that for lengthscales larger than scale L, buoyancy forces are important in the flow and act to suppress the scale of the density straining. Itsweire *et al.* (1986), introduced a buoyancy lengthscale $L_b \sim w/N$ and we note that our definition in (13) can be related to their lengthscale by assuming the r.m.s vertical velocity w is of the same order as the Kolmogorov velocity scale $(\nu\varepsilon)^{1/4}$.

Substituting (13) into (12) yields

$$K_\rho \sim \frac{\varepsilon}{N_*^2} \sim \nu\left(\frac{\varepsilon}{\nu N_*^2}\right). \tag{14}$$

Equation (14) is valid for $L_B < L < L_K$, equivalent to the condition $\kappa N_*^2 < \varepsilon < \nu N_*^2$. In the limit that L approaches L_B, K_ρ approaches the laminar value κ. Although the result in (14) is similar in form to equation (8), the prediction from the buoyancy-flux-based arguments leading to (8) is that in this regime with $\varepsilon < \nu N_*^2$ the buoyancy flux b is zero and hence the effective diffusivity equals the laminar value κ throughout this regime. The result in (14) is thus fundamentally different.

4.2.3. *Energetic density-stratified turbulence*

A third regime exists if we consider the case where the displacement scales L are larger than L_K. Buoyancy forces will act to suppress overturning of any scales that are

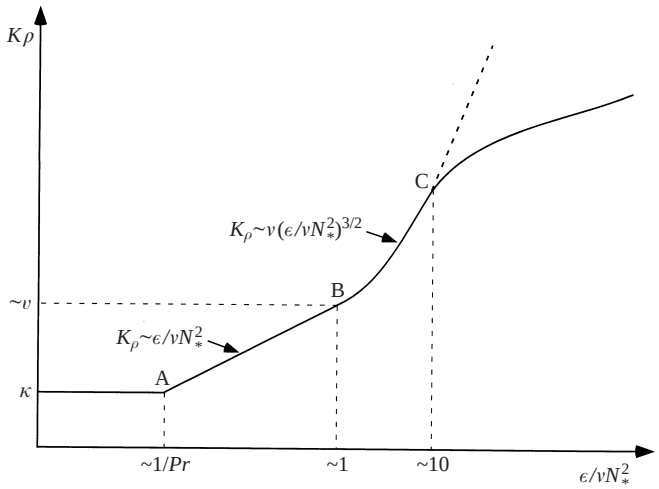

FIGURE 7. Schematic of vertical eddy diffusivity K_ρ as a function of $\varepsilon/\nu N_*^2$ showing the regimes predicted by the model, ranging from laminar to energetic density-stratified turbulence.

larger than the Ozmidov scale $L_O = (\varepsilon/N_*^3)^{1/2}$. An upper bound can thus be obtained by setting $L \sim L_O$ into (12) yielding

$$K_\rho \sim \left(\frac{\varepsilon}{\nu N_*^2}\right)^{1/2} \frac{\varepsilon}{N_*^2} \sim \nu \left(\frac{\varepsilon}{\nu N_*^2}\right)^{3/2}. \tag{15}$$

Equation (15) is valid for $L_O > L_K$, i.e. when $\varepsilon > \nu N_*^2$. In the limit when ε approaches νN_*^2, the two results (14) and (15) agree. While the final expressions for the eddy diffusivity K_ρ in the two regimes in (14) and (15) are independent of the molecular diffusivity κ, the earlier general result in (12) emphasizes the fundamental linear relationship between K_ρ and κ.

4.2.4. *Very energetic or unstratified turbulence*

The model leading to equation (12) assumes that during the straining or wrapping of isopycnal surfaces depicted in figure 6, the background density field is 'frozen' in the sense that the density contrast in (11) is always proportional to the background density gradient $\mathrm{d}\rho/\mathrm{d}z_*$. If the fluid was initially unstratified, then clearly (11) is not defined and the model is not applicable in the unstratified limit. There is a second more subtle possibility even if the fluid is intially stratified. If $\varepsilon > 15\nu N_*^2$ there can be a non-zero density flux $\overline{\rho' w'}$ within the eddy. In the time it takes for the eddy to rollup the isopycnals, this density flux could therefore weaken the local density gradient within the eddy. This means that the density contrast estimated in (11) would be an upper bound, implying the eddy diffusivity estimate in (12) would also be an upper-bound estimate. In practice we therefore expect that once $\varepsilon > 15\nu N_*^2$ the result in (15) will be an upper-bound estimate and the observed eddy diffusivities K_ρ will asymptotically approach the expected unstratified limit of $K_\rho - \varepsilon^{1/3} L^{4/3}$ as $\varepsilon/\nu N_*^2 \to \infty$.

4.2.5. *Summary and application of the model*

In figure 7 we show a schematic representation of the predictions of the above model in the regimes that we have delineated in terms of the value of the parameter $\varepsilon/\nu N_*^2$. The model is based on scaling arguments and experimental data are required

to test the model and accurately define regime boundaries. The points A, B and C represent the transitions between regimes. At point B the estimate of the eddy diffusivity is $K_\rho \sim \nu$. For a temperature-stratified fluid, this is only $O(10^1)$ times the diffusivity at point A, but for a salt-stratified fluid point B corresponds to an increase of $O(10^3)$ in K_ρ over the molecular value at point A. Beyond point C when $\varepsilon/\nu N_*^2$ becomes large and approaches the unstratified limit, we expect the model to fail and to overestimate the actual diffusivity shown as the solid line. On the other hand, the model predictions should become increasingly accurate as $\varepsilon/\nu N_*^2$ decreases and the turbulence approaches the diffusive limit. As figure 7 shows, the model predicts a smoothly increasing value of the eddy diffusivity over the entire range.

How then does this model help us to interpret the experimental measurements? The design of the present experiments did not allow us to independently measure the eddy diffusivity K_ρ and the dissipation. The observation from figure 3 is that, in the BBL, $\varepsilon \approx \nu N_*^2$. Hence the prediction from figure 7 is that $K_\rho \sim \nu \sim 10^{-6}\,\mathrm{m^2\,s^{-1}}$, three orders of magnitude greater than the molecular diffusivity for salt of $\kappa = 10^{-9}\,\mathrm{m^2\,s^{-1}}$. From § 3.1, there is a large difference between the background laminar dissipation rate and the turbulent dissipation rate in the boundary layer (figure 3 *a*), which is physically consistent with this predicted range of diffusivities. The benthic layer is therefore predicted to be highly turbulent, consistent with our qualitative observations.

For moderate turbulent intensities, equation (14) agrees with the scaling often assumed by oceanographers, namely that $K_\rho = \Gamma(\varepsilon/N_*^2)$ where Γ is interpreted as a constant mixing efficiency of $\Gamma = 0.2$ (e.g. Munk & Wunsch 1998). Because we have not measured the rate of change of background potential energy in these experiments, we can offer no further insight into the value of Γ. For energetic turbulence, however, when $\varepsilon > \nu N_*^2$ the scaling results indicate that K_ρ has an additional dependence on the intensity measure $(\varepsilon/\nu N_*^2)^{1/2}$. The range of validity of this expression remains to be determined from experiments.

5. Conclusions

We have considered the case of mixing in a benthic boundary layer on a slope which is energized by a beam of internal waves in a continuously stratified fluid. A simple model of the energetics in the boundary layer region yields a prediction of the rate of dissipation of turbulent kinetic energy ε in good agreement with direct measurements. The results imply that even for non-critical waves, a large fraction of the incident energy is lost upon reflection at a sloping boundary.

Our results are in the range where $\varepsilon/\nu N^2 \sim O(1)$. This is low for typical oceanic values, but such values are often found in lakes (e.g. Imberger & Ivey 1991; Saggio & Imberger 2000). In this regime, analysis of the measured rates of dissipation and density flux showed that the results could not be fully explained by existing models describing the relationship between dissipation rate ε, the density flux and the eddy diffusivity K_ρ. We have, therefore, devised a simple model to describe the mixing using a definition based on the diascalar flux, as outlined in the earlier work of Winters & D'Asaro (1996). We have derived scaling relations for the eddy diffusivity K_ρ which exhibit consistent asymptotic limits and provide a description for turbulent mixing in three flow regimes ranging from laminar to energetic density-stratified turbulence. Our results are consistent with the notion that the eddy diffusivity depends on three parameters: the strength of the background stratification N_*, the strength of the turbulent dissipation rate ε, and the value of the kinematic viscosity ν. Interestingly, when the flow is turbulent, the results are always independent of the molecular diffusivity κ.

Future work needs to address the simultaneous measurement of the turbulent dissipation rate ε and the eddy diffusivity K_ρ, computed from the actual rate of change of the background potential energy, in order to test the predictions of the simple model outlined here.

The authors wish to thank Jörg Imberger for his constructive suggestions and for making the Portable Flux Probe (PFP) available for this study. Nicky Grigg helped undertake some of the early experiments. Stewart Turner, David Luketina and Eric Kunze provided valuable comments on an initial draft of this manuscript, as have the anonymous reviewers. This work was supported by the Australian Research Council, the Centre for Environmental Fluid Dynamics and with partial support from the Office of Naval Research. This forms CWR reference ED1279.

REFERENCES

Batchelor, G. K. 1959 Small-scale variation of convected quantities like temperature in a turbulent fluid. Part 1. General discussion and the case of small conductivity. *J. Fluid Mech.* **5**, 113–133.

Bendat, J. S. & Piersol, A. G. 1966 *Measurement and Analysis of Random Data*. J. Wiley and Sons.

Cacchione, D. & Wunsch, C. 1974 Experimental study of internal waves over a slope. *J. Fluid Mech.* **66**, 223–239.

De Silva, I. P. D., Imberger, J. & Ivey, G. N. 1997 Localised mixing due to a breaking internal wave ray at a sloping bed. *J. Fluid Mech.* **350**, 1–27 (referred to herein as DII).

Eriksen, C. C. 1982 Observations of internal wave reflection off sloping bottoms. *J. Geophys. Res.* **87**, 525–538.

Eriksen, C. C. 1985 Implications of ocean bottom reflection for internal wave spectra and mixing. *J. Phys. Oceanogr.* **15**, 1145–1156.

Etemad-Shahidi, A. & Imberger, J. 1998 Anatomy of turbulence in a thermally stratified lake. *Limnol. Oceanogr.* (submitted).

Grigg, N. & Ivey, G. N. 1997 A laboratory study of the dynamics and mixing in a salt wedge estuary. *Geophys. Astrophys. Fluid Dyn.* **85**, 65–95.

Imberger, I. & Hamblin, P. F. 1982 Dynamics of lakes, reservoirs and cooling ponds. *Ann. Rev. Fluid Mech.*, **14**, 153–187.

Imberger, J. & Head, R. 1994 Measurements of turbulent properties in a natural system. In *Fundamentals and Advancements in Hydraulic Measurements and Experimentation*, pp. 1–20. ASCE.

Imberger, J. & Ivey, G. N. 1991 On the nature of turbulence in a stratified fluid: Part 2: Application to lakes. *J. Phys. Oceanogr.* **21**, 659–680.

Itsweire, E. C., Helland, K. N. & Van Atta, C. W. 1986 The evolution of grid-generated turbulence in a stably stratified flow. *J. Fluid Mech.* **162**, 299–338.

Ivey, G. N., De Silva, I. P. D. & Imberger, J. 1995 Internal waves, bottom slopes and boundary mixing. *Aha Hulikoa, Hawaiian Winter Workshop on Topographic Effects in the Ocean. Honolulu, Hawaii* (ed. P. Muller & D. Henderson), pp. 199–205. School of Ocean and Earth Science Special Publication.

Ivey, G. N. & Imberger, J. 1991 On the nature of turbulence in a stratified fluid: Part 1: The energetics of mixing. *J. Phys. Oceanogr.* **21**, 649–658.

Ivey, G. N., Imberger, J. & Koseff, J. R. 1998 Buoyancy fluxes in a stratified fluid. In *Physical Processes in Lakes and Oceans* (ed. J. Imberger), pp. 311–318. AGU Press.

Ivey, G. N. & Nokes, R. I. 1989 Vertical mixing due to the breaking of critical internal waves on sloping boundaries. *J. Fluid Mech.* **204**, 479–500.

Ivey, G. N. & Nokes, R. I. 1990 Mixing driven by the breaking of internal waves against sloping boundaries. *Proc. Intl Conf. on Physical Modelling of Transport and Dispersion, MIT, Boston* (ed. E. E. Adams & G. E. Hecker), pp. 11A3–11A8.

Ledwell, J. R. & Hickey, B. M. 1995 Evidence for enhanced boundary mixing in the Santa Monica basin. *J. Geophys. Res.* **100**, 665–679.

Lemckert, C. & Imberger, J. 1995 Turbulent boundary layers in fresh water lakes. *IUTAM Symp. on Physical Limnology, Broome, Western Australia*, pp. 409–422.

Luketina, D. & Imberger, J. 1998 Determining turbulent kinetic energy dissipation from Batchelor curve fitting. *J. Atmos. Ocean. Tech.* (submitted).

Michallet, H. & Ivey, G. N. 1999 Experiments on mixing due to internal solitary wave breaking on uniform slopes. *J. Geophys. Res.* **104**, 13467–13478.

Munk, W. & Wunsch, C. 1998 Abyssal recipes II: energetics of tidal mixing and wind mixing. *Deep-Sea Res.* I **45**, 1977–2010.

Osborn, T. R. 1980 Estimates of the local rate of vertical diffusion from dissipation measurements. *J. Phys. Oceanogr.* **10**, 83–89.

Phillips, O. M. 1977 The Dynamics of the Upper Ocean. Cambridge University Press.

Saggio, A. & Imberger, J. 2000 Mixing and turbulent fluxes in the metalimnion of a stratified lake. *Limnol. Oceanogr.* in press.

Sun, H., Kunze, E. & Williams, A. J. 1996 Vertical heat-flux measurements from a neutrally buoyant float. *J. Phys. Oceanogr.* **26**, 984–1001.

Taylor, J. R. 1993 Turbulence and mixing in the boundary layer generated by shoaling internal waves. *Dyn. Atmos. Oceans* **19**, 233–258.

Teoh, S. G., Ivey, G. N. & Imberger, J. 1997 Laboratory study of the interactions between two internal wave rays. *J. Fluid Mech.* **336**, 91–122.

Thorpe, S. A. 1987 On the reflection of a train of finite amplitude internal waves from a uniform slope. *J. Fluid Mech.* **178**, 299–302.

Thorpe, S. A., Hall, P. & White, M. 1990 The variability of mixing on a continental slope. *Proc. R. Soc. Lond* A **439**, 115–130.

Toole, J. M., Polzin, K. L. & Schmitt, R. W. 1994 Estimates of diapycnal mixing in the abyssal ocean. *Science* **264**, 1120–1123.

Van Haren, H., Oakey, N. & Garrett, C. 1994 Measurements of internal wave band eddy fluxes above a sloping bottom. *J. Mar. Sci.* **52**, 909–946.

White, M. 1994 Tidal and subtidal variability in the sloping benthic boundary layer. *J. Geophys. Res.* **99**, 7851–7864.

Winters, K. B. & D'Asaro, E. A. 1996 Diascalar flux and the rate of fluid mixing. *J. Fluid Mech.* **317**, 179–193.

Wolanski, E. 1987 Some evidence for boundary mixing near coral reefs. *Limnol. Oceanogr.* **32**, 735–739.

Wuest, A., Van Senden, D. C., Imberger, J., Piepke, G. & Gloor, M. 1994 Diapycnal diffusivity measured by microstructure and tracer techniques – A comparison. *Intl Symp. on Stratified Flows, Grenoble, France*, vol. 3, p. B5–8.